Research Square

Preprints are preliminary reports that have not undergone peer review.
They should not be considered conclusive, used to inform clinical practice,
or referenced by the media as validated information.

The Turkish Tsunami of 6 February 2023 in the Northeastern Mediterranean

Alisa Medvedeva (alisa.bannikova@gmail.com)
Shirshov Institute of Oceanology RAS
Danil Vydrin
Shirshov Institute of Oceanology RAS
Artem Krylov
Shirshov Institute of Oceanology RAS
Arina Shiryborova
Shirshov Institute of Oceanology RAS
Daria Smirnova
Shirshov Institute of Oceanology RAS
Elizaveta Tsukanova
Shirshov Institute of Oceanology RAS
Utku Kânoğlu
Dokuz Eylül University
Igor Medvedev
Shirshov Institute of Oceanology RAS

Research Article

Keywords: tsunami observations, Mediterranean Sea, tide gauges, earthquake, air pressure, Gulf of İskenderun, Pazarcık earthquake, seiches

Posted Date: May 22nd, 2023

DOI: https://doi.org/10.21203/rs.3.rs-2928701/v1

License: This work is licensed under a Creative Commons Attribution 4.0 International License.
Read Full License

Version of Record: A version of this preprint was published at Pure and Applied Geophysics on September 25th, 2023. See the published version at https://doi.org/10.1007/s00024-023-03341-8.

Abstract

Two powerful earthquakes struck southeastern Turkey on 6 February 2023 with the magnitudes of M_w = 7.8 and M_w = 7.5 in nine hours. In addition, a storm surge caused by the passage of a cyclone over the area coincided with the first earthquake. Field observations showed that the fault planes did not extend to the Mediterranean Sea; however, a weak tsunami was observed on several tide gauges in the northeastern Mediterranean. Historically, there were tsunamis in the Levantine Sea region caused by earthquakes on land within the East Anatolian Fault Zone and the Dead Sea, having a complex cause, i.e., earthquakes and associated landslides. Hence, we studied the origin of the generated waves. We separated and estimated various components of sea level oscillations from 1 to 8 February 2023, using spectral and f-t analyses and sets of narrow-band and high-frequency filters. The earthquake M_w = 7.8 on 6 February 2023 caused a weak tsunami with maximum amplitudes 15–17 cm in Erdemli and Arsuz. We identified that the increase in sea level oscillations in Arsuz after 7 February was associated with the impact of the cyclone. The maximum amplitude of sea level oscillations, 22 cm, in Arsuz was observed on 7 February and is associated with infragravity waves caused by the influence of storm surge during the passage of the cyclone. In Erdemli, on the contrary, the influence of high-frequency waves of atmospheric origin is significantly lower, i.e., the amplitude of the sea level oscillations after 7 February was less than 10 cm.

Introduction

On 6 February 2023 at 01:17:35 UTC, the catastrophic Pazarcık earthquake of Kahramanmaraş earthquake sequence with a magnitude M_w = 7.8 occurred in southeastern Turkey and northern Syria, to the East of Nurdağı at 26 km (37.174°N, 37.032°E). The hypocenter depth was ~ 10 km according to USGS. About nine hours later (10:24:49 UTC), the second strong earthquake (Elbistan earthquake) with a magnitude M_w = 7.5 occurred in the same region, province of Gaziantep (USGS), near 4 km SSE of Ekinözü (38.024°N, 37.203°E). The number of aftershocks caused by these two earthquakes reached ~ 6 040 as of 20.02.2023. As of 08.03.2023 at least 50 500 casualties, ~ 115 000 injured, about 1.5 million people made homeless; at least 164 000 buildings destroyed or severely damaged and 150 000 commercial infrastructure moderately damaged in 10 provinces across Turkey (Syria/Turkey Earthquakes Situation Report #7, 2023). At least 7 259 casualties, ~ 14 500 were injured and 5.37 million people were homeless; at least 490 buildings were destroyed and thousands damaged in northwestern Syria (Syria/Turkey Earthquakes Situation Report #7, 2023).

During the last 36 centuries, 67 earthquakes with $M > 7$, 133 earthquakes with $7 > M > 6$, and at least 96 tsunamis were documented in the Eastern Mediterranean (Yalciner et al., 2007). Onshore and offshore earthquakes occurring in the northeastern and eastern sectors of the Levantine Sea region have generated tsunamis in the past. Most of the events in the Levantine Basin are related to the boundary of the African, Arabian, and Anatolian tectonic plates. Six earthquakes: ~1365 BC, 115, 1404, 1114, 1752, and 1872 AD events, are known tsunamigenic within the East-Anatolian fault zone (Altinok et al., 2011).

The seismic source of the first earthquake caused a small tsunami with a maximum amplitude[1] of 17 cm. They were revealed in tide gauge records and *f-t* diagrams at six stations on the Turkish coast. The main goal of the presented study was to analyze all available tide gauge records on the Levantine Sea, to evaluate the statistical and spectral properties of observed sea level oscillations, and to identify tsunami waves. We revealed tsunami signals on six records of tide gauge stations and separated the meteorological impact from it.

Seismotectonic of the region

The earthquake of 6 February occurred along the East Anatolian Fault zone, which has a length of ~ 450–700 km (Çetin et al. 2023; Güvercin et al., 2022), and adjacent faults at the contact of the Arabian and Anatolian tectonic plates near their triple junction with the African plate (Fig. 1). It generated large, destructive earthquakes with $M > 6.5$ in the past. The right-lateral North Anatolian Fault and the left-lateral East Anatolian Fault are the main structures of regional importance in the recent tectonics of the Eastern Mediterranean. The Anatolian microplate is located between them and moves westward under the influence of internal deformation caused by the collision of the Arabian and African plates with the Eurasian plate (Emre et al., 2018). The southwestern end of the Anatolian Fault zone transfer into the Cyprus Island Arc and the meridional Levant transform zone (Dead Sea fault zone). In the northeastern part, the zone intersects with the North Anatolian fault zone and is limited by the Bitlis-Zagros Fold and Thrust Belt. Late Quaternary active faults are mostly of a north-easterly strike and left-lateral strike-slip, occasionally with thrust and normal components. Slip values vary from 1–4 mm/year for western segments to 10 mm/year for segments located at the eastern end of the fault zone (Güvercin et al., 2022).

The field observations indicate that the Kahramanmaraş earthquakes' sequence is the result of rupturing of the fault zones with a length of the main M_w = 7.8 earthquake ~ 300 km with major surface displacements on the order of 3–7 m (Çetin et al. 2023). It corresponds to the Erkenek, Pazarcık, and Amanos segments of the East Anatolian Fault Zone (Emre et al., 2018; Hancılar et al., 2023). For the Elbistan earthquake (M_w7.5), the total rupture length is around 160 km with major surface displacements on the order of 2–8 m. According to USGS finite fault solution, as of 05 April 2023, the maximum slip value for the Pazarcik earthquake at the first segment, where initially started rupturing, was 1.9 m. In the second segment, its maximum was 11.2 m, and for the third segment 8.2 m. The focal mechanism solutions of both earthquakes indicate a left-lateral strike-slip (USGS). As for 20.04.2023, finite fault decision (USGS) consists of three segments north with strike 60° and south with strike 25°. The maximum slip value in the north more extended segment was 3.36 m, but this part of the slip distribution was entirely located on land. In the second segment, its maximum was 1.56 m. The epicenter of the second earthquake with a magnitude M_w = 7.5 was at a greater distance from the seacoast. Table 1 shows the main parameters and fault-plane solutions of these two earthquakes.

Table 1
Main parameters and fault-plane solutions of the two Turkish catastrophic earthquakes (USGS)

Date and time (UTC)	Magnitude, M_W	Seismic moment (Nm)	Latitude (°N)	Longitude (°E)	Depth (km)	Strike (°)	Dip (°)	Rake (°)
2023-02-06 01:17:35	7.8	5.39e20	37.17	37.04	10	318	89	-179
						228	89	-1
2023-02-06 10:24:49	7.5	2.64e20	38.02	37.20	13.1	277	78	4
						186	87	168

As a result of the earthquake with M_w = 7.8, the maximum recorded peak ground accelerations (PGA) were 0.8 g for the horizontal component and 0.85 g for the vertical component. The PGA values computed using the relations (Chiou et al., 2014) are in the range from 0.013 g to 1.3 g for various epicentral distances. Estimated shaking intensity according to the scale (Bilal et al., 2014) ranges from 4.2 to 11.6 (Hancılar et al., 2023).

Earthquake sources located within the Eastern Mediterranean region also historically generated tsunamis of various intensities. In the tsunami catalog (Altinok et al., 2011) since ~ 1365 BC, 30 tsunamigenic events have been recorded with a reliability of ≥ 2 (questionable) for the northern, northwestern, and eastern sectors of the Levantine Sea (Altinok et al., 2011). Among them 18 of the tsunami events are located along the coast of the Levant: eight events are generated by onshore earthquakes (525 and 590 BC, 859, 1170, 1404, 1408, 1822, and 1872 AD), eight events are related to offshore earthquakes (~ 1365 and 140 BC, 115, 551, 1114, 1752 and two events in 1759 AD), other two events could be generated by earthquakes with epicenter situated both on land and at sea (991, 1202 AD). For some events, the contribution of seismogenic landslides to tsunami generation is possible (115, 859, 991, 1202, and 1759 AD). For three events, the contribution of seismogenic landslides to tsunami generation was established (551, 1404, and 1408 AD).

For the Cyprus Island Arc zone, eight tsunami events are known, and all of them are associated with offshore earthquake sources. For the southern coast of Minor Asia, four events are known, three of which were generated by underwater earthquakes (68, 1403, 1743 AD). For the event 1036/1037 AD, the location of the tsunamigenic earthquake epicenter is not well determined.

Analysis of meteorological processes

The earthquake coincided with a cyclone over the Anatolian Peninsula. We used the hourly mean sea level pressure (MSLP) and 10-m winds during for period 1–7 February 2023 for the analysis of the meteorological processes. These data were obtained from ERA5 (fifth-generation records of the ECMWF atmospheric reanalyzes of the global climate; Hersbach et al. 2020). The gyre was generated on 3

February from the Icelandic Low and the center of this atmospheric structure moved from west to east along the southern Turkish shoreline. The minimal pressure value in the cyclone was 991 hPa and wind speed (hereafter 10-m winds will be described) increased to 70 $km \cdot h^{-1}$ (19.4 $m \cdot s^{-1}$) on its periphery. After separation, the gyre was transferred over the northern part of the Northern Sea and crossed Central Europe in the southeastern direction from the Danish Straits to the Sea of Marmara (4 February, 21:00 UTC). Above this region, pressure rose to 1012 hPa and wind speed fell to 40 $km \cdot h^{-1}$ (11 $m \cdot s^{-1}$). Three hours later, on 5 February, 00:00 UTC, atmospheric pressure over the Aegean Sea started to drop down from 1012 hPa, and by 21:00 UTC it had been around 997 hPa. The cyclone's center shifted to the east (Fig. 2a). Wind speed went up to 72 $km \cdot h^{-1}$ (20.0 $m \cdot s^{-1}$) on the periphery over the central part of the Aegean Sea. Such high values haven't been observed for the following days.

Pressure dropped by another 1 hPa in the cyclone center a few minutes before the earthquake (6 February, 01:00 UTC, Fig. 2b). Wind speed and direction to the southeast of Cyprus played an important role in sea level oscillations in some cities. Here maximum speed value was 59 $km \cdot h^{-1}$ (16.4 $m \cdot s^{-1}$), and the wind had a northeastern general direction, toward the Gulf of Arsuz. The wind wasn't so strong at the entry of the bay due to geographic location, some features of coastal relief, and wind direction near the shore. Wind speed didn't exceed 28 km h^{-1} (7.8 m s^{-1}). Pressure increased to 998 hPa in the gyre's center for the next 5 hours (6 February, 01:00 UTC, Fig. 2c). Wind speed fell to 55 $km \cdot h^{-1}$ (15.4 $m \cdot s^{-1}$), but in a similar direction to the southeast of Cyprus. At the same time, the wind became stronger on the sea boundary of the Gulf of İskenderun (36 km h^{-1}, or 10.0 m s^{-1}). Generally, wind speed gradually lowered over the eastern part of the Mediterranean Sea. The cyclone center was over the Gulf of Arsuz six hours later (6 February, 01:00 UTC, Fig. 2d). The pressure didn't increase (998 hPa); however, wind speed rose again to the southeast of Cyprus (58 $km \cdot h^{-1}$, or 16.2 $m \cdot s^{-1}$). It might have caused a cyclone northward moving and the southern periphery was also transported. The wind regime remained the same. When the gyre had been moving eastward, its area increased. During the following 12 hours low-pressure structure had propagated to the eastern part of the Black Sea. As a result, the second core was generated over that region. Pressure evenly rose to 1002 hPa over the Gulf of İskenderun. Values grew to 1010 hPa on 7 February, 12:00 UTC. The cyclone continued its propagation to the east.

Analysis of sea level observations

We used sea level records from six tide gauges on the Mediterranean Sea coast of southern Turkey for the detailed time series analysis. The stations are located westward from the earthquake epicenter: Arsuz, Erdemli, Taşucu, Bozyazı, Antalya, and Marmaris as shown in Fig. 3, with the wave parameters listed in Table 2. We obtained the 30-second sea level records from the Intergovernmental Oceanographic Commission (IOC) from 1 January to 7 February 2023. The observations are homogeneous, i.e., all data series have a time step Δt = 30 seconds, a vertical resolution is 1 mm, and correspond to the Greenwich Meridian time (UTC). We checked the series thoroughly and eliminated all spikes and shifts. We also filled in short gaps with linear interpolation.

Table 2
Maximum wave amplitudes (cm) on tide gauge stations and calculated tsunami arrival times generated by the M_w = 7.8 earthquake using the wavefront orientation method of Fine and Thomson (2013).

Station	°N	°E	Maximum wave amplitude (cm)	Calculated arrival time (min)
Arsuz	36.58	36.18	15	0–20
Erdemli	36.61	34.31	17	1 h 28
Taşucu	36.32	33.88	6	1 h 39
Bozyazı	36.10	32.98	13	1 h 39
Antalya	36.89	30.70	2	2 h 7
Marmaris	36.85	28.26	5	2 h 35

Sea level oscillations (ζ_{tot}) may be considered as

$$\zeta_{tot} = \zeta_0 + \zeta_{tid} + \zeta_{res}$$

1

,

where ζ_0 is the mean sea level, ζ_{tid} is the tide, and ζ_{res} is the residual nonperiodic sea level oscillations. Furthermore, we analyzed the residual sea level records, which can be considered as the sum of low-frequency (ζ_{LF}) and high-frequency (ζ_{HF}) sea level components;

$$\zeta_{res} = \zeta_{LF} + \zeta_{HF},$$

2

where ζ_{LF} is a meteorologically induced sea level component that includes storm surges. Moreover, the high-frequency oscillations ζ_{HF} can be represented as the sum of individual components of different origins as

$$\zeta_{HF} = \zeta_{sei} + \zeta_{tsu} + \zeta_{IG}.$$

3

Here, ζ_{sei}, ζ_{tsu}, and ζ_{IG} represent seiche, tsunami, and infra-gravitational (IG) wave components, respectively. Separating these components is not a trivial task.

Natural oscillations of gulfs and bays (seiches) can be excited by a wide range of different oceanic and atmospheric processes. In the case of the eastern part of the Mediterranean Sea, atmospheric pressure disturbances and squall lines, as well as the penetration of tsunami waves from the open sea can generate seiches. Extreme seiches with atmospheric origin are commonly associated with

meteotsunamis (Monserrat et al. 2006). IG waves are formed through the nonlinear interaction of wind waves and swell; the most intensive IG wave formation occurs in the coastal wave-breaking zone, where these waves are known as surf beats (Munk 1949; Battjes 1988). Typical periods of seiches are from a few minutes to a few hours, while conventional periods of IG waves are an order of magnitude shorter (30–300 s). The frequency bands of seiches and IG waves partly overlap, impeding their separation in our analyses. The spectral properties of the two processes are different (Medvedev et al. 2020), and the IG waves can be distinguished from atmospherically-induced seiches.

High- and low-frequency and f-t analysis

We applied the approach described above to each station, i.e., carried out the time series analysis in several stages considering the components of sea level oscillations. The eastern part of the Mediterranean Sea is a micro-tidal area. The mean spring tidal range $2(H_{M_2} + H_{S_2})$, in this part of the sea, is about 0.3 m. Earthquakes occurred during the syzygy, and the tidal range reached up to 0.38 m in Erdemli and up to 0.43 m in Arsuz (Fig. 4a–b). First, we subtracted tides from the original sea level records using the least squares method (Pawlowicz et al., 2002).

Then, a high-pass filter was used with a 3-hour Hamming window to separate ζ_{LF} and ζ_{HF} oscillations (Fig. 4 and Fig. 5). Figure 4 shows ζ_{HF} oscillations at Arsuz (Fig. 4c) and Erdemli (Fig. 4d) after the subtraction of tides (ζ_{tid}) and storm surges (ζ_{LF}). These records show sharp changes in the sea level character at 1:00–2:00 UTC on 6 February. The arrival of the tsunami corresponds to a low tide.

High-frequency records of sea level oscillations for all the stations are given in Fig. 5 and their *f-t* diagrams are presented in Fig. 6. We used the wavefront orientation method of Fine and Thomson (2013) for the calculation of tsunami arrival time (Table 2). It is based on Huygens' Principle and uses an eight-point grid-point pattern. The calculated tsunami arrival time varies from 0–20 min in Arsuz to 2 hours 35 min in Marmaris, which is the most remote among the analyzed gauges (Fig. 3).

The highest wave amplitudes were observed at Erdemli (17 cm) and Arsuz (15 cm) at two stations closest to the epicenter. The high-frequency sea level (ζ_{HF}) record at Arsuz shows significant noise before the earthquake. Sea level oscillations caused by an earthquake begin at Arsuz almost instantly with the earthquake at 01:17:35 UTC (Fig. 5). There is an immediate increase in the variance of ζ_{HF} oscillations in the 12-min period, as shown on the corresponding *f-t* diagram. The range of ζ_{HF} increases over time, reaching a maximum at the end of 7 February. This is most likely due to the meteorological impact since the tsunami wave from such an initial disturbance was weak.

The tsunami signal is seen in the corresponding *f-t* diagram for Erdemli at a 6-min period. For this period, the intensification of ζ_{HF} oscillations persists for slightly more than a day. In Taşucu, the *f-t* diagram showed a ζ_{HF} oscillation component with a period of 60 min that was before the earthquake. After the earthquake, this oscillation increased and the signal intensity was maintained for almost a day. There is also a fluctuation with a 15–20 min period, which occurs after the tsunami arrival time and quickly

attenuates. At Bozyazı, after the tsunami arrival time the oscillation with a period of 8–10 min increases. The intensification persists for slightly less than a day. In Taşucu, the maximum ζ_{HF} range was 6 cm, while in Bozyazı, it was 13 cm. The calculated tsunami arrival times for these two locations are the same, 1 hour 39 min, but the character of the tsunami signal manifestation in the records and on the *f-t* diagrams differs.

At the two stations farthest from the source, Antalya and Marmaris, it is impossible to distinguish a tsunami wave in the sea level records; the tsunami signal appears only on *f-t* diagrams (Fig. 6). In Antalya, the calculated tsunami arrival time is 2 h 7 min. The oscillations there intensified with the period of 30 min after the arrival of the tsunami. This period corresponds to the eigenperiod (seiche) of the bay, as the strengthening persisted there for two days and it was manifested there before the earthquake. However, after the arrival of the tsunami, the intensification became evident. At Marmaris, we observed a ζ_{HF} oscillation with a period of 30 min, and the eigenmode is also visible on the sea level records. However, after the arrival of the tsunami (2 h 35 min), the variance of this ζ_{HF} oscillation intensifies. The maximum wave amplitude recorded in Marmaris was 5 cm, while in Antalya it was 2 cm.

We also considered tide gauges located farther than Marmaris along the Turkish, Greek, and Italian coasts. However, the tsunami signal did not appear either on tide gauge records or *f-t* diagrams, likely due to a weak initial disturbance. There is no available data on the closer coasts, i.e., in Israel or Egypt, although the wave could have been observed there. Also, the tide gauge record at Gazimagusa (Famagusta, Northern Cyprus) was presented in Çetin et al. (2023). The tsunami wave amplitude there reached 17 cm, and waves arrived there 65 minutes after the earthquake. Any signature from the second earthquake does not appear in any way either in the tide gauge records or the *f-t* diagrams.

Spectral analysis

The sea level measurements were divided into two parts to study the spectral properties of the sea level oscillations during earthquakes on 6 February:

(1) the 7 days, 19–25 January 2023, corresponding to background sea level variations before the event; and

(2) the 24 hours, 6 February 2023, for sea level oscillations during the tsunami.

We applied spectral analysis by the Welch method based on the fast Fourier transform. The spectra were calculated using the Kaiser-Bessel spectral window with a length of N = 1024 measurements, with a half overlapping on the 30-second sea level data (Fig. 7). The full length of the background sea level record (7-day period) was 20 160 measurements, the tsunami record (24-hour period) had a length of 2 880 measurements. The number of degrees of freedom for the background spectra was v = 76, and for the tsunami, the spectra was v = 8.

In addition, the source functions were calculated (Fig. 8), which quantify the amplification of the event spectrum relative to background conditions (Rabinovich 1997):

$$R(\omega) = \frac{S_{ts}(\omega)}{S_{bg}(\omega)}$$

4

.

All spectra show an increase in spectral density across the entire frequency range. However, the distant stations exhibit weak spectral density at high frequencies (Fig. 7). For instance, Antalya is characterized by an increase in energy relative to the background level at frequencies up to 10 cycles per hour (cph) (Fig. 7e).

The spectral analysis results (Fig. 7) are in good agreement with the *f-t* analysis. Spectral peaks with 86, 39, and 16–11 min periods are observed at the Arsuz (Fig. 7a), which is also well traced in the *f-t* analysis. Furthermore, the increase of spectral energy in the background spectrum at all frequencies was observed. At the Erdemli station (Fig. 7b), spectral peaks with periods of 20, 6.6, and 1.5 min stand out sharply. At the Taşucu station (Fig. 7c), oscillations exhibit with 60, 22, and 9.7 min are well-pronounced periods. The Bozyazı station (Fig. 7d) is characterized by oscillations with 13, 2.3, and 1.8 min periods. On the day of the earthquake, the Antalya station (Fig. 7e) did not experience strong changes in the background spectrum of sea level oscillations. However, the fluctuations with periods of 30 and 12 min showed themselves more significant than usual; an increase in energy is observed only in the low-frequency part of the spectrum. There are also weak changes at the Marmaris station (Fig. 7f), perhaps oscillations with periods of 37, 16, and 9.6 min showed themselves slightly more pronounced than usual.

Discussion

The earthquake coincided with a storm surge in the eastern Mediterranean Sea. Figure 9a–b show the time series of residual sea level oscillations (ζ_{res}) at Arsuz and Erdemli including, the low-frequency component (ζ_{LF}) of the sea level variations (with period $T > 3$ h), which is the storm surge. The storm surge height above the mean sea level reached 0.2 m. At Arsuz, a low-frequency seiche with a period of about 3–4 h is seen (Fig. 9a). The first tsunami waves were observed just at the moment when the storm surge reached its maximum values. In Fig. 9c–d, records of sea level oscillations ζ_{HF} after high-pass filtering ($T < 3$ h) are shown, similar to those shown in Fig. 5 but in a shorter time frame. The main difference between the records at Arsuz and Erdemli is the nature of the attenuation of sea level oscillations caused by the tsunami. At Erdemli, the amplitude of ζ_{HF} significantly decreases within 12 hours after the earthquake, and the standard deviation of σ (ζ_{HF}) after 12:00 UTC on 6 February is only 1.6 times higher than the σ (ζ_{HF}) for the recording interval before the earthquake, for example, from 12:00 on 5 February to 00:00 on 6 February. In Arsuz, the situation is quite different. The ζ_{HF} energy after the arrival of tsunami waves not only does not die out but also continues to increase. Thus, the σ (ζ_{HF})

before the tsunami was 2.1 cm, in the first 12 hours of the tsunami it was about 5.3 cm, and after 12:00 UTC on 6 February, it increased to 5.9 cm. Figure 9e–f show the non-periodic sea level oscillations ζ_{bp}, selected using a narrow-band filter with periods from 6 min to 3 h. The sea level record for Erdemli is practically the same as the record in Fig. 9d, while the record for Arsuz differs significantly from Fig. 9c. Thus, the σ(ζ_{bp}) was 1.9 cm before the tsunami, was about 4.7 cm in the first 12 h of the tsunami, and it decreased to 3.2 cm after 12:00 UTC on 6 February. The difference between Fig. 9c and Fig. 9e are fluctuations with a period of less than 6 min. These oscillations are IG waves and partly high-frequency modes of natural bays' oscillations.

Figure 10 shows the time series of high-frequency sea level fluctuations ζ_{HF} from 31 January, 00:00 to 8 February, 00:00 for Arsuz. In the time series ζ_{HF}, an enhancement in the following time frames can be distinguished starting from A1–31.01, 19:00 UTC, A2–1.02, 17:20 UTC, and A3–6.02, 1:00 UTC. All three selected areas of the time series are well manifested in the enhancement of ζ_{HF} on the *f-t* diagrams (Fig. 10a). The maximum amplitudes ~ 24 cm (the height ~ 52 cm) of ζ_{HF} occurred on the evenings of 1 and 7 February. The total high-frequency sea-level oscillations ζ_{HF} (Fig. 10b) are divided into two components using a narrow-band filter:

1. Narrow-band signal ζ_{bp}in the range of periods *T* from 6 min to 3 h (Fig. 10c). This part of the spectrum of sea-level fluctuations is formed by tsunami waves ζ_{tsu} and seiches ζ_{sei}. Moreover, natural oscillations of the sea level of bays could be excited both by the passage of a cyclone and by the arrival of tsunami waves.
2. The highest frequency component ζ_{IG}, associated with IG waves and surf beats, with periods less than 6 min (Fig. 10d).

The ζ_{bp} time series reach its maximum values (Fig. 10c) immediately after a catastrophic M_w = 7.8 earthquake on 6 February 2023 at 01:17:35 UTC (Area A3). This can be interpreted as the occurrence of a tsunami wave in Arsuz Bay with an amplitude of about 15 cm and a height of ~ 26 cm. After an earthquake, the energy of sea level oscillations decays. At the end of 1 February (A2), we also see some increase in the variance ζ_{bp}, but it has a different character of signal amplification. The case of 6 February (tsunami, A3) has a sharp onset, after which the signal decays for tens of hours, while on 1 February (A2) the signal ζ_{bp} has an envelope that can be approximated by a Gaussian function. The *f-t* diagrams confirm our hypothesis. The tsunami on the morning of 6 February (A3) manifested itself in sea level oscillations mainly in the form of a narrow-band signal with periods of 10–20 min, and for longer and shorter periods, the energy of ζ_{bp} is much weaker. In the case of events on the night of 31 January to 1 February (A1), as well as in the afternoon of 1 February (A2), the ζ_{bp} intensified in a wide range of periods from several minutes to an hour, and the higher the oscillation frequency, the higher the variance. Such an *f-t* structure of the spectrum is typical for sea level oscillations caused by the passage of cyclones (see Medvedev et al., 2022). On the curve ζ_{IG} with periods less than 6 min (Fig. 10d), the sea level oscillations after the earthquake increase slowly and reach their maximum values in the morning and evening of 7 February, the amplitude up to 19 cm and the height ~ 46 cm.

Conclusions

Much attention in the media was paid to the "flood," which was observed in the eastern side of the Arsuz fishery port within a few days after the M_w = 7.8 earthquake on 6 February 2023. The observations and evidence obtained during the field survey identified that the reason was the subsidence of the coastal area behind the fishery port during the earthquake shaking most probably due to the liquefaction (Çetin et al. 2023). At high tide, seawater gradually invaded the subsided area and could not be drained because of the collapsed surface water drainage system.

Pazarcık earthquake with the M_w = 7.8 on 6 February 2023 caused a tsunami. The tsunami was weak, but its signal was detected in the sea level records and it was well distinguishable in their *f-t* diagrams. The maximum tsunami wave amplitude was 17 cm in Erdemli and 15 cm in Arsuz. No tsunami was detected in sea level records from the second Elbistan earthquake, unlike the first one.

Yalciner et al. (2023) numerically simulated this tsunami on 6 February 2023. A tsunami source was set as elliptical subsidence of 1m at maximum with 12×8 km dimensions along the coast of the Gulf of İskenderun. This study is prepared by analysis of the wave arrival times and amplitudes recorded by the three tide gauges (Arsuz, Erdemli, and Gazimagusa/Famagusta) in the area and modeling several alternatives for a preliminary assessment.

On February 6, a complex pattern of sea level variability was observed on the eastern coast of the Mediterranean Sea. The occurrence of tsunami waves coincided with the peak of the storm surge and high-frequency sea level oscillations caused by the passage of a cyclone over the area from 5–7 February. We separated and estimated various components of sea level oscillations that were observed in the eastern Mediterranean during the period from 1 to 8 February, using spectral and *f-t* analyses and various sets of narrow-band and high-frequency filters.

So the increase in sea level oscillations in Arsuz after 7 February was associated with the impact of the cyclone, and not with the tsunami caused by the M_w = 7.8 earthquake on 6 February 2023. The maximum amplitude of sea level oscillations, 22 cm, in Arsuz was observed on 7 February and is associated with infragravity waves caused by the influence of storm surge during the passage of the cyclone. In Erdemli, on the contrary, the influence of high-frequency waves of atmospheric origin is significantly lower, the amplitude of the sea level oscillations after February 7 was less than 10 cm.

The Kahramanmaraş earthquake of 6 February and the associated tsunami event is not unique to the Levantine region. Earthquake sources situated within East-Anatolian fault zones generated tsunamis of various intensities in the past. Tsunami generation by the earthquake sources situated onshore with strike-slip mechanism is a challenging task requiring for further study.

Declarations

Funding.

This study was supported by the Russian State Assignment of IORAS FMWE-2021-0004.

References

1. Altinok, Y., Alpar, B., Özer, N., & Aykurt, H. (2011). Revision of the tsunami catalogue affecting Turkish coasts and surrounding regions. *Natural Hazards and Earth System Sciences*, 11(2), 273-291.
2. Altinok, Y., Ersoy, Ş. (2000). Tsunamis Observed on and Near the Turkish Coast. In: Papadopoulos, G.A., Murty, T., Venkatesh, S., Blong, R. (eds) *Natural Hazards. Springer*, Dordrecht. https://doi.org/10.1007/978-94-017-2386-2_5
3. Bachmanov D.M., Kozhurin A.I., Trifonov V.G. The active faults of Eurasia database. *Geodynamics & Tectonophysics* 2017, 8(4), 711-736. (In Russ.) https://doi.org/10.5800/GT-2017-8-4-0314
4. Battjes, J. A. Surf-zone dynamics. *Ann. Rev. Fluid Mech.* **20**, 257–293 (1988).
5. Bilal M., Askan A. Relationships between Felt Intensity and Recorded Ground-Motion Parameters for Turkey. *Bulletin of the Seismological Society of America* 2014, 104(1), 484–496. https://doi.org/10.1785/0120130093
6. Çetin, K., M. Ilgaç, G. Can, E. Çakır (eds.) (2023) Preliminary Reconnaissance Report on February 6, 2023 Kahramanmaraş-Pazarcık (Mw=7.7) and Elbistan (Mw=7.6) Earthquakes, METU/EERC 2023-01, METU - Earthquake Engineering Research Center, pp. 91.
7. Chiou B. S.-J., Youngs R.R. Update of the Chiou and Youngs NGA Model for the Average Horizontal Component of Peak Ground Motion and Response Spectra. *Earthquake Spectra* 2014, 30(3), 1117-1153. https://doi.org/10.1193/072813EQS219M
8. Earthquake response in Türkiye and Whole of Syria. World Health Organization flash appeal. Available online: https://cdn.who.int/media/docs/default-source/documents/emergencies/2023/who_flashappeal_earthquakeresponse_11-feb-2023.pdf?sfvrsn=94d4de2a_1 (accessed on 12 February 2023).
9. Emre, Ö., Duman, T.Y., Özalp, S., Şaroğlu, F., Olgun, Ş., Elmacı, H., Çan, T. Active fault database of Turkey. *Bulletin of Earthquake Engineering* 2018, 16(8), 3229-3275. https://doi.org/10.1007/s10518-016-0041-2.
10. Flanders Marine Institute (VLIZ); Intergovernmental Oceanographic Commission (IOC) (2023): Sea level station monitoring facility. Accessed at http://www.ioc-sealevelmonitoring.org on 2023-02-21 at VLIZ. DOI: 10.14284/482.
11. Güvercin, S. E., Karabulut, H., Konca, A. Ö., Doğan, U., & Ergintav, S. (2022). Active seismotectonics of the East Anatolian Fault. *Geophysical Journal International*, *230*(1), 50-69. https://doi.org/10.1093/gji/ggac045
12. Hancılar U., Şeşetyan K., Çaktı E., Yenihayat N., Süleyman H., Açıkgöz N., Dede S., Acar S. Kahramanmaraş - Gaziantep Türkiye M7.7 Earthquake, 6 February 2023 (04:17 GMT+03:00), Strong Ground Motion and Building Damage Estimations Preliminary Report (v5). Available online: https://www.emsc-csem.org/Doc/Additional_Earthquake_Report/1218444/Kahramanmaras-

Gaziantep_Earthquake_06-02-2023_(04.17)-Bogazici_University_Earthquake_Engineering_Department.pdf (accessed on 14 February 2023).

13. Hersbach, H., and Coauthors, 2020: The ERA5 global reanalysis. Quart. J. Roy. Meteor. Soc., 146, 1999–2049, https://doi.org/10.1002/qj.3803.
14. Kasapoglu K.E., Toksöz M.N. Tectonic consequences of the collision of the Arabian and Eurasian plates: finite element models. In: M. Friedman and M.N. Toksöz (Editors), Continental Tectonics: Structure, Kinematics and Dynamics. *Tectonophysics* 1983, 100, 71-95.
15. Medvedev, I. P., Rabinovich, A. B., & Šepić, J. (2022). Destructive coastal sea level oscillations generated by Typhoon Maysak in the Sea of Japan in September 2020. *Scientific Reports*, *12*(1), 8463.
16. Monserrat, S., Vilibić, I. & Rabinovich, A. B. Meteotsunamis: Atmospherically induced destructive ocean waves in the tsunami frequency band. *Nat. Hazard. Earth Sys. Sci.* 6, 1035-1051; https://doi.org/10.5194/nhess-6-1035-2006 (2006).
17. Munk, W. H. Surf beats, *Eos Trans. Amer. Geophys. Un.* 30, 849-854 (1949).
18. PRESS BULLETIN-29 about the Earthquake in Kahramanmaraş. Ministry of Interior of the Republic of Türkiye Disaster and Emergency Management Authority. Available online: https://en.afad.gov.tr/press-bulletin-29-about-the-earthquake-in-kahramanmaras (accessed on 14 February 2023).
19. Rabinovich, A.B. Spectral analysis of tsunami waves: Separation of source and topography effects. J. Geophys. Res. 1997, 102, 12663–12676.
20. Syria/Turkey Earthquakes Situation Report #7, March 8, 2023. International Medical Corps Situation update https://reliefweb.int/report/syrian-arab-republic/syriaturkey-earthquakes-situation-report-7-march-8-2023
21. USGS. Available online: https://earthquake.usgs.gov/earthquakes/search/ (accessed on 11 February 2023).
22. Yalciner A. C. et al. Modeling and visualization of tsunamis: Mediterranean examples //Tsunami and Nonlinear Waves. – 2007. – P. 273-283.
23. Yolsal, S., Taymaz, T., & Yalçiner, A. C. (2007). Understanding tsunamis, potential source regions and tsunami-prone mechanisms in the Eastern Mediterranean. Geological Society, London, Special Publications, 291(1), 201-230.

Footnotes

1. Here and further, we consider “amplitude” as the zero-to-peak value, and “height” as the trough-to-crest value (about double amplitude)

Figures

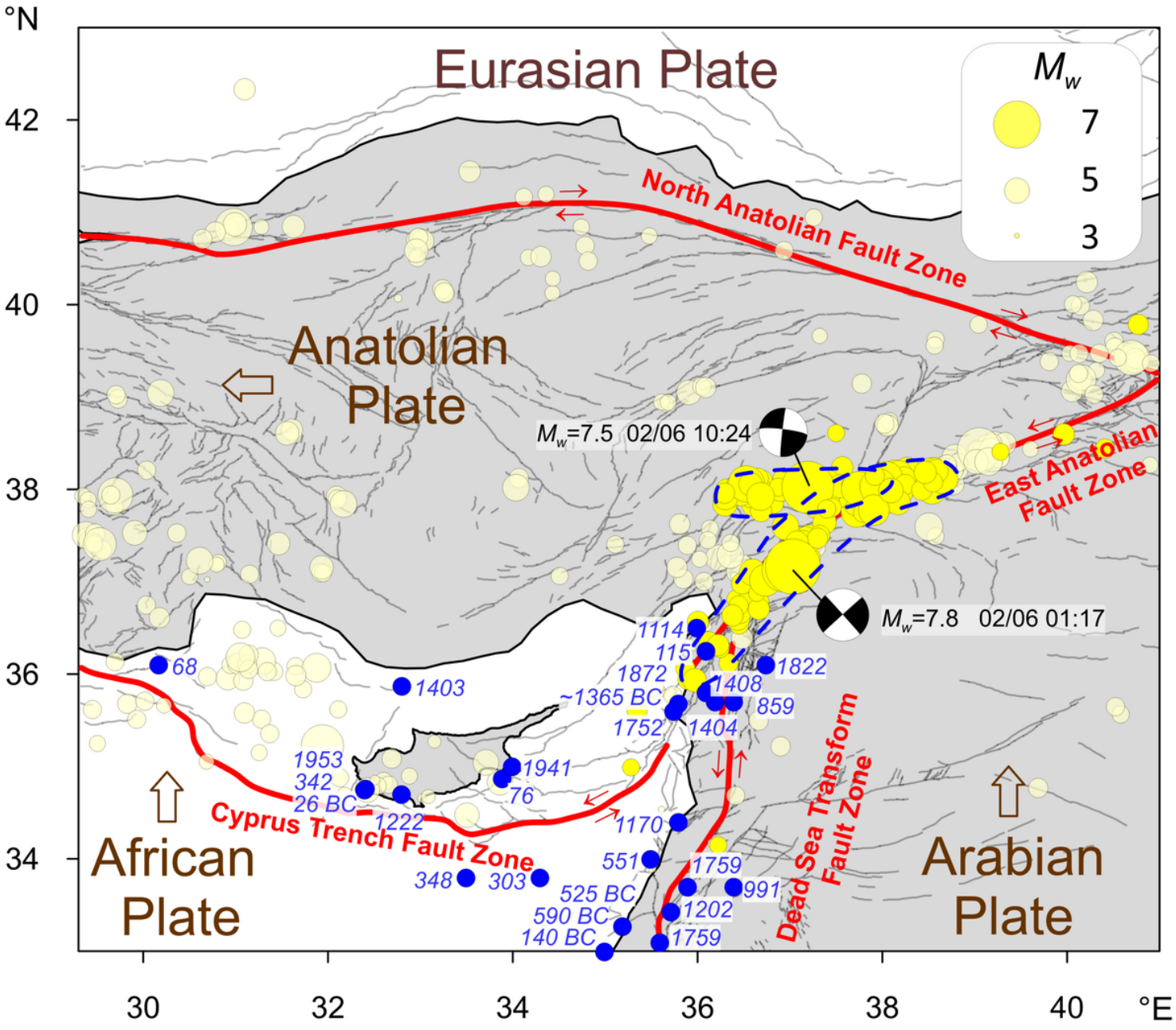


Figure 1

Map of the Anatolian region showing regional tectonic settings, the epicenters, and focal mechanisms of the catastrophic earthquakes that occurred on 6 February 2023 at 01:17:35 UTC (M_W = 7.8) and at 10:24:49 UTC (M_W = 7.5) (USGS) major fault zones (thick red lines) and minor active faults distribution (thin gray lines) (Emre et al., 2018; Bachmanov et al., 2017; Kasapoglu and Toksöz, 1983), regional earthquakes epicenters with M_W > 3 (pale yellow circles – for the 5 years before 6 February 2023, and bright yellow circles – for the period 6–10 February 2023) (USGS). Brown arrows indicate the general directions of movement of tectonic plates while red arrows – the direction of movement along the major fault zones (Emre et al., 2018; Kasapoglu and Toksöz, 1983). Blue circles indicate tsunamigenic earthquakes of the past according to (Altinok et al., 2011, Yolsal et al., 2007).

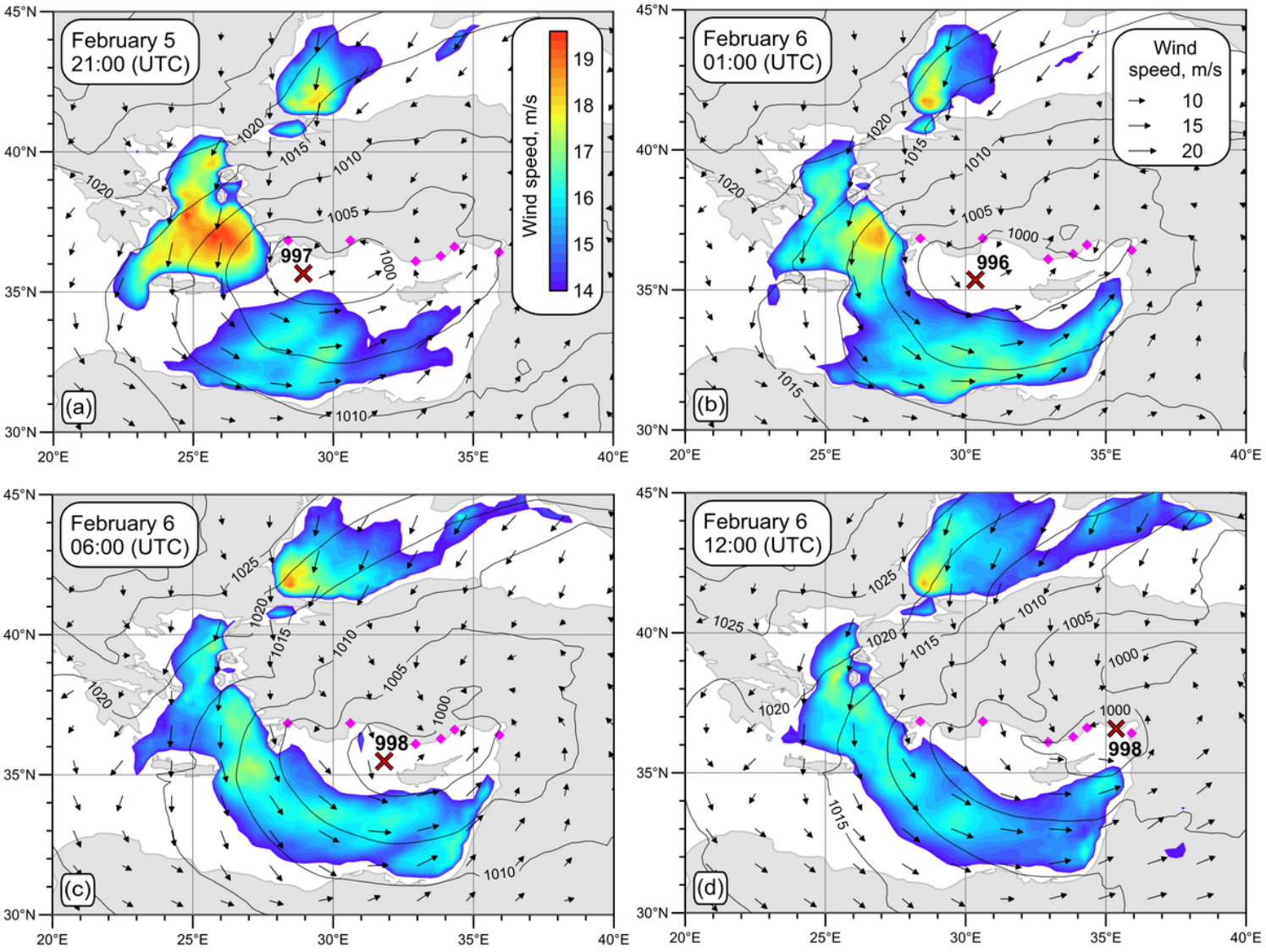


Figure 2

The ERA5 atmospheric pressure (black isolines) and 10-m wind velocity (colored areas) fields, at (a) 21:00 UTC on 5 February, (b) 01:00 UTC on 6 February, (c) 06:00 UTC on 6 February, (d) 12:00 UTC on 6 February. Symbol (x) marks the cyclone's center. The bold text shows the pressure values (hPa) in the cyclone center. Isobars are given with the 5-hPa step. Only wind speeds higher than 14 m/s are colored. Arrows show the direction and value of wind velocity, pink squares indicate tide gauges location.

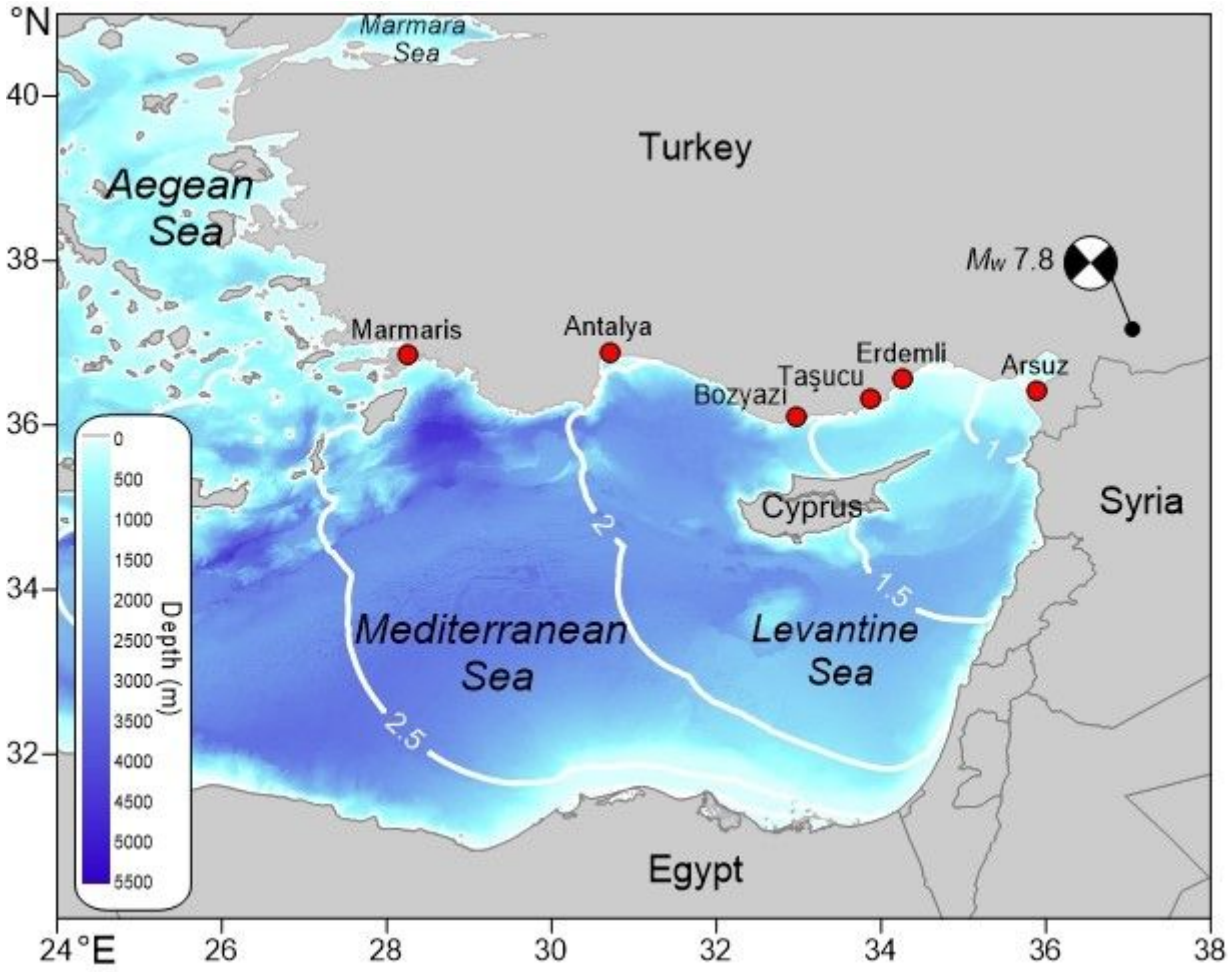


Figure 3

The location of the tide gauge stations (red circles), the bathymetry of the region, and the calculated arrival time of the tsunami (white isolines) from the time of the first earthquake (hours) using the wavefront orientation method (Fine and Thomson, 2013).

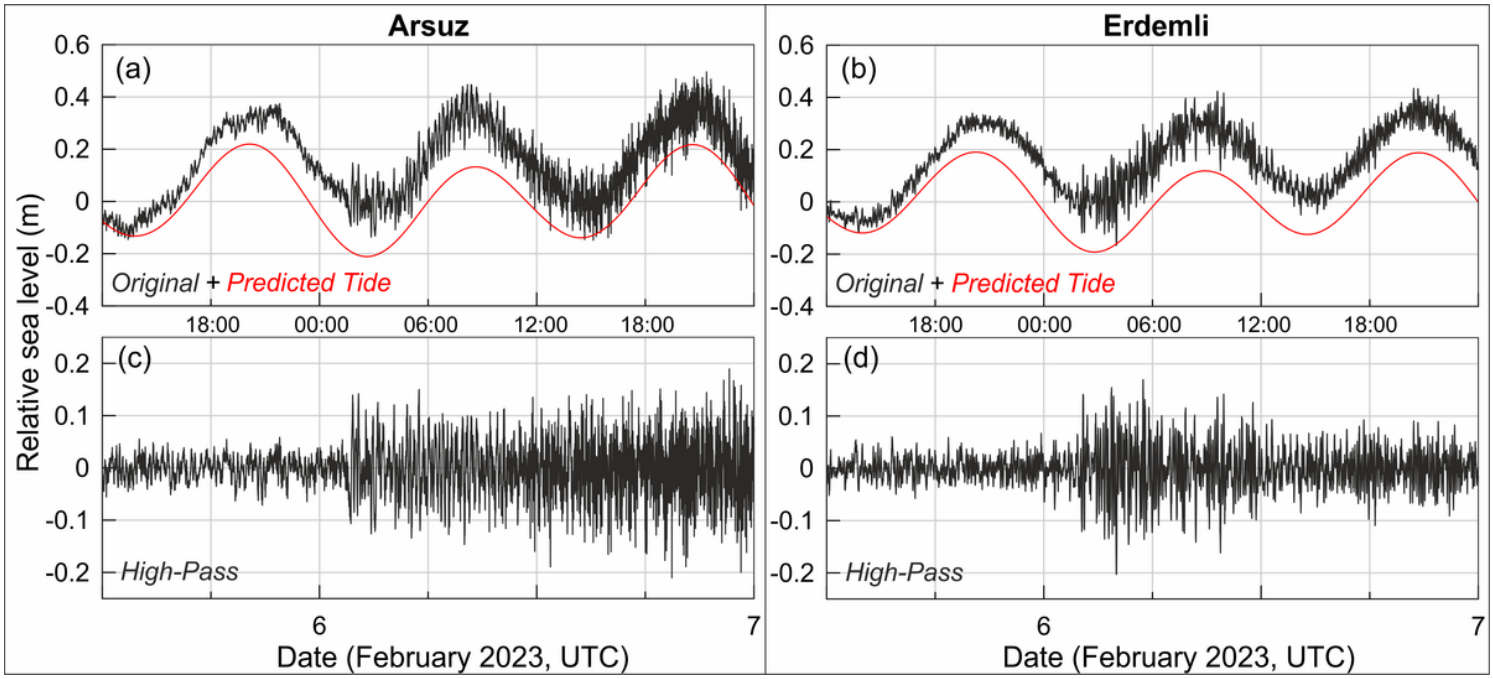


Figure 4

Original (initial) sea level records at (a) Arsuz and (b) Erdemli, the red solid line shows the predicted tide. High-frequency sea level records at (c) Arsuz and (d) Erdemli.

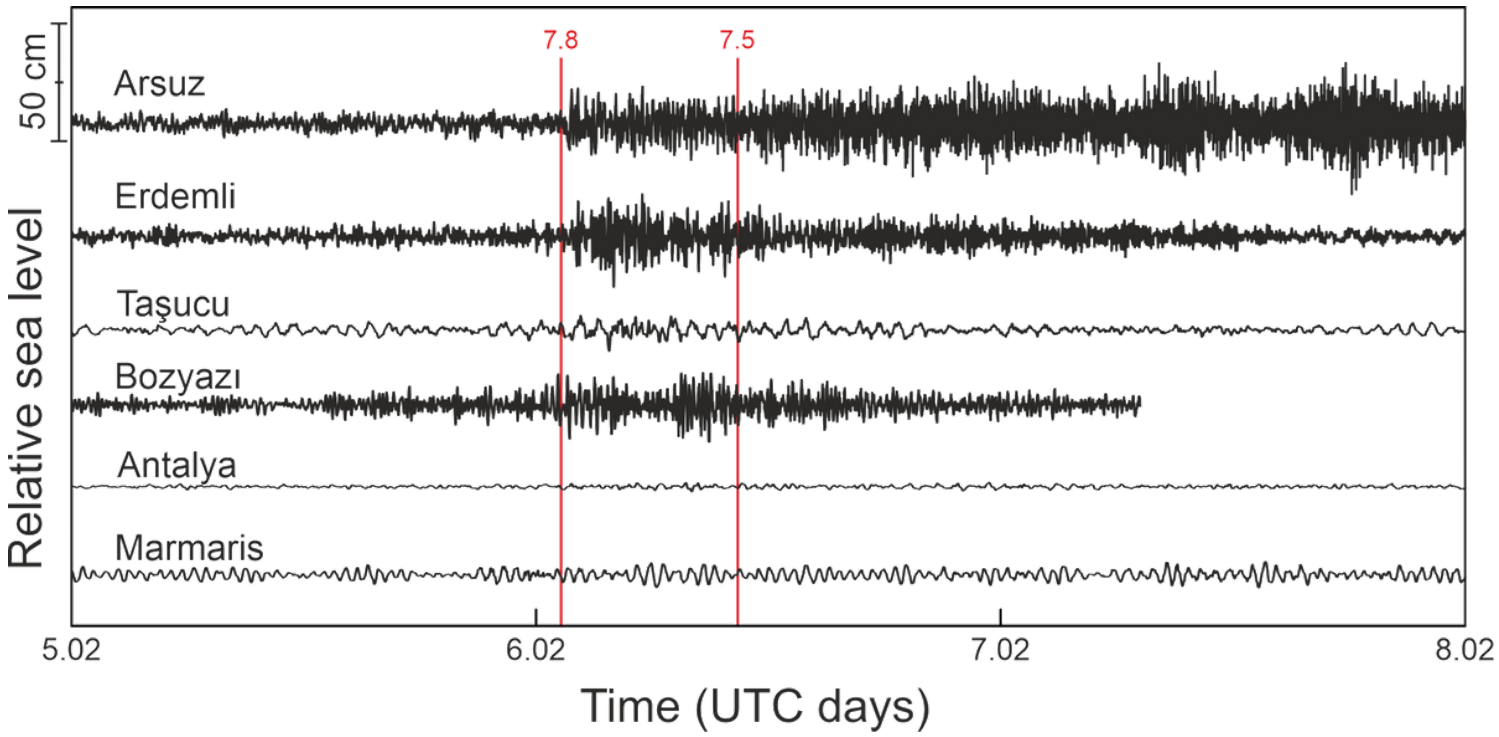


Figure 5

High-frequency sea level records at Arsuz, Erdemli, Taşucu, Bozyazı, Antalya, and Marmaris for the period of 5–7 February 2023. The solid vertical lines indicate the times of the M_w = 7.8 (01:17:35 UTC) and M_w = 7.5 (10:24:49 UTC) earthquakes.

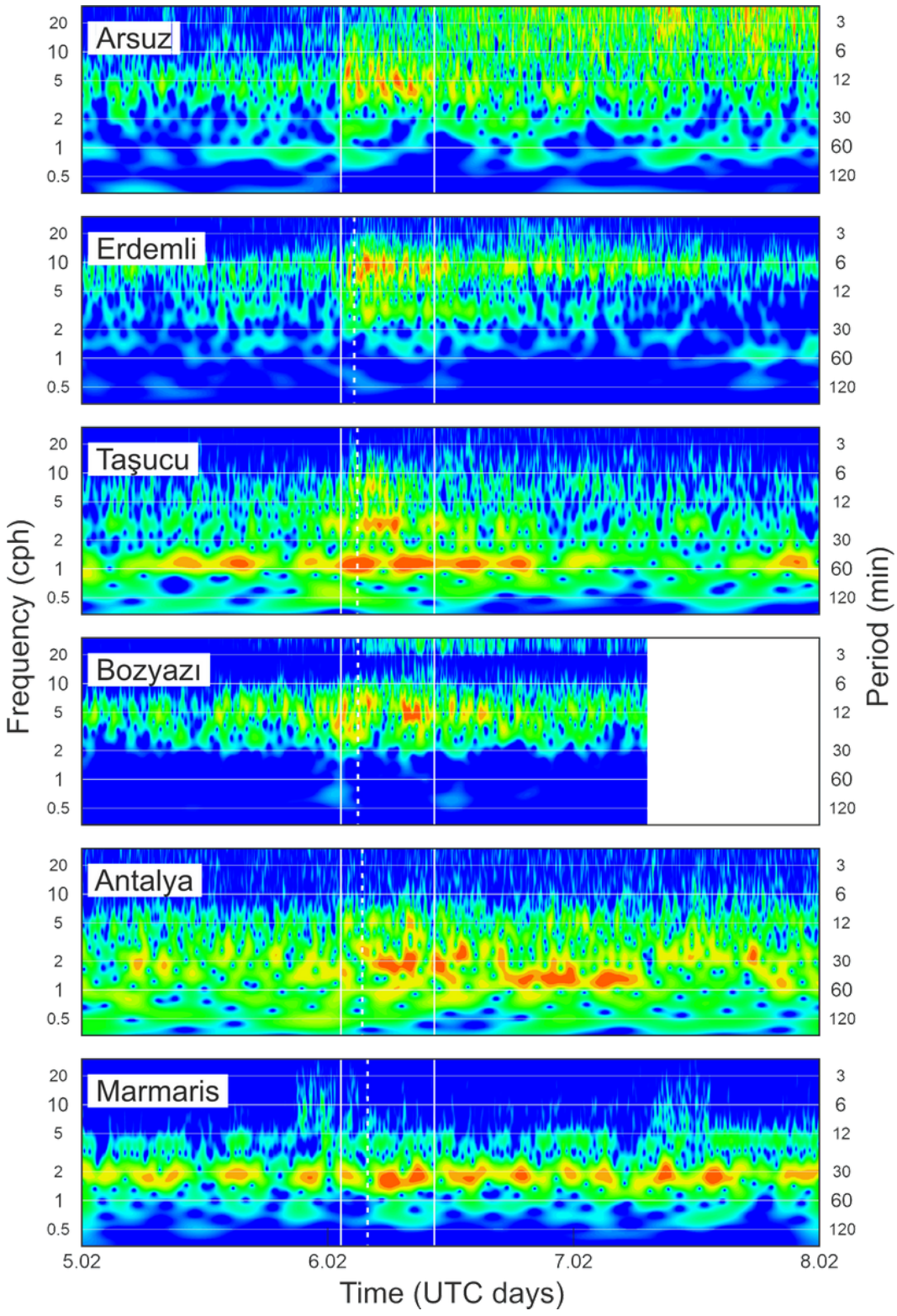


Figure 6

F-t diagrams of the high-frequency sea level records at Arsuz, Erdemli, Taşucu, Bozyazı, Antalya, and Marmaris for the period of 5–7 February 2023. The solid vertical lines indicate the times of the M_w = 7.8 (01:17:35 UTC) and M_w = 7.5 (10:24:49 UTC) earthquakes and the dashed white line represents the calculated tsunami arrival time generated by the M_w = 7.8 earthquake. Bozyazı record is shorter because the tide gauge had large gaps and then stopped working at all.

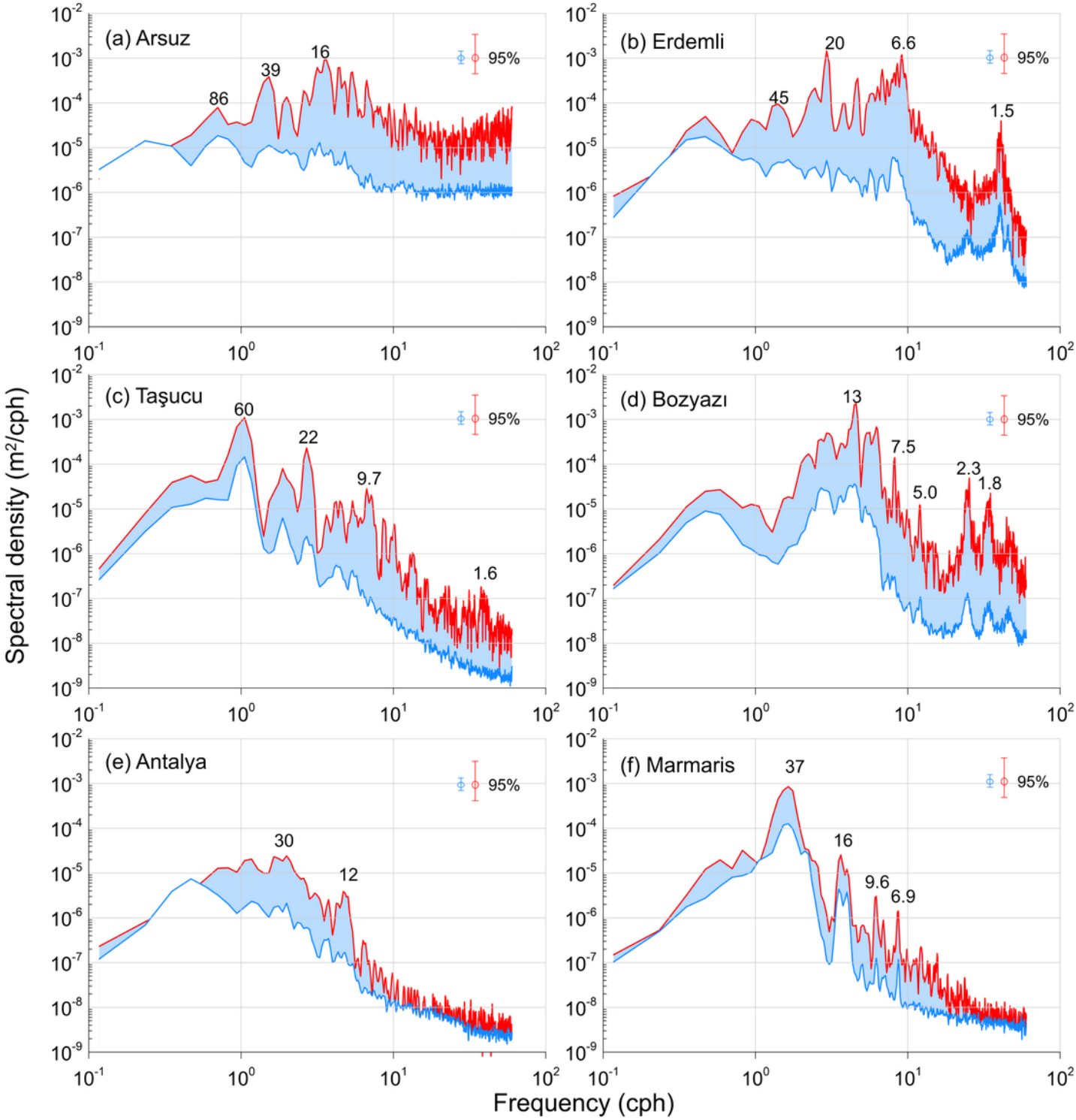


Figure 7

Spectra of background (pre-tsunami) and 2023 tsunami sea level oscillations at (a) Arsuz, (b) Erdemli, (c) Taşucu, (d) Bozyazı, (e) Antalya, and (f) Marmaris. Background spectra are shown in blue, and the tsunami spectra are shown in red. Periods (in min) of the main spectral peaks are indicated. The shaded areas denote the energy of tsunami-generated oscillations.

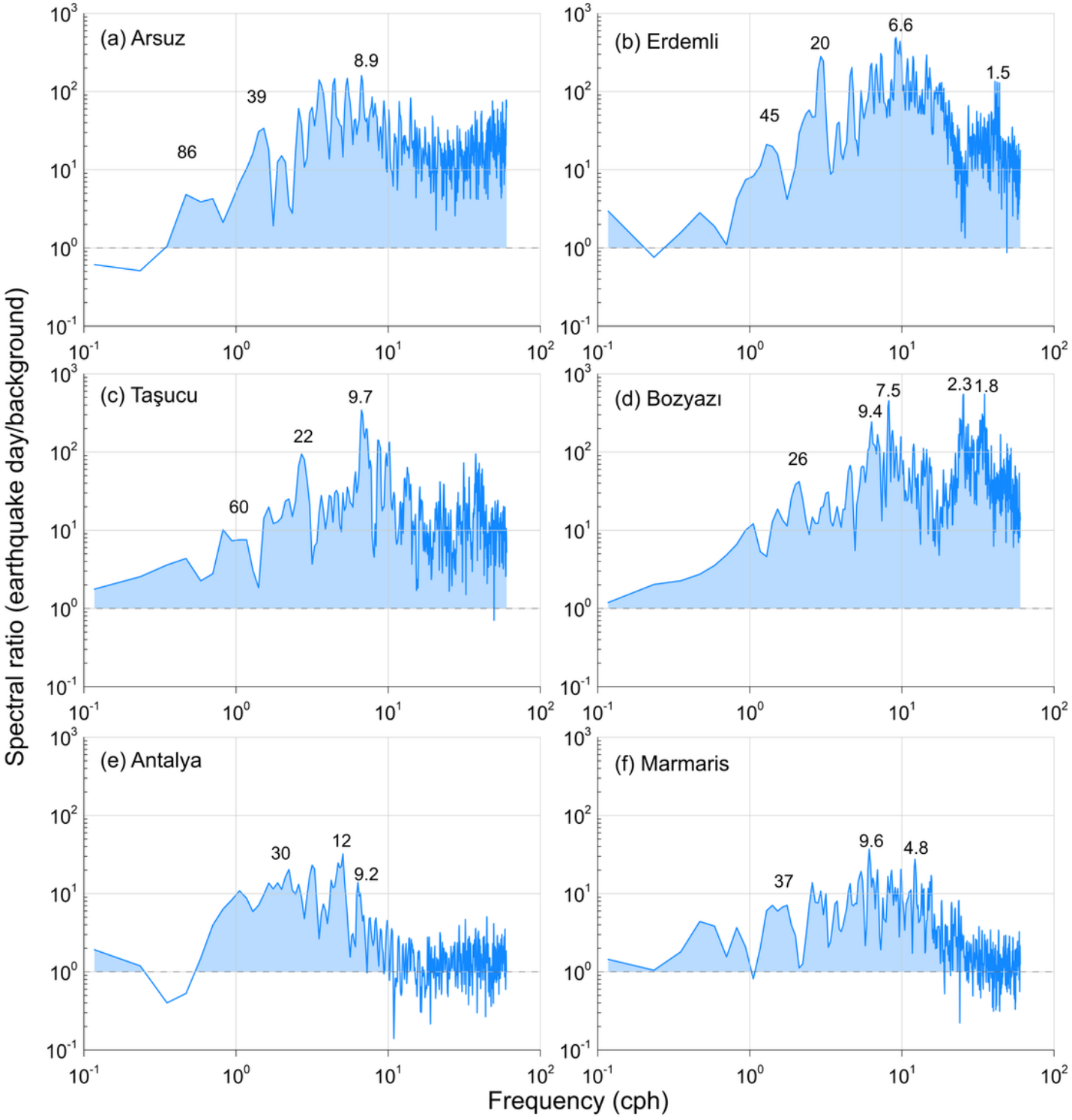


Figure 8

Ratios of the tsunami spectra to the background spectra, R(ω), at (a) Arsuz, (b) Erdemli, (c) Taşucu, (d) Bozyazı, (e) Antalya, and (f) Marmaris. The shaded areas are the amplification on the day of earthquake spectra relative to the background spectra.

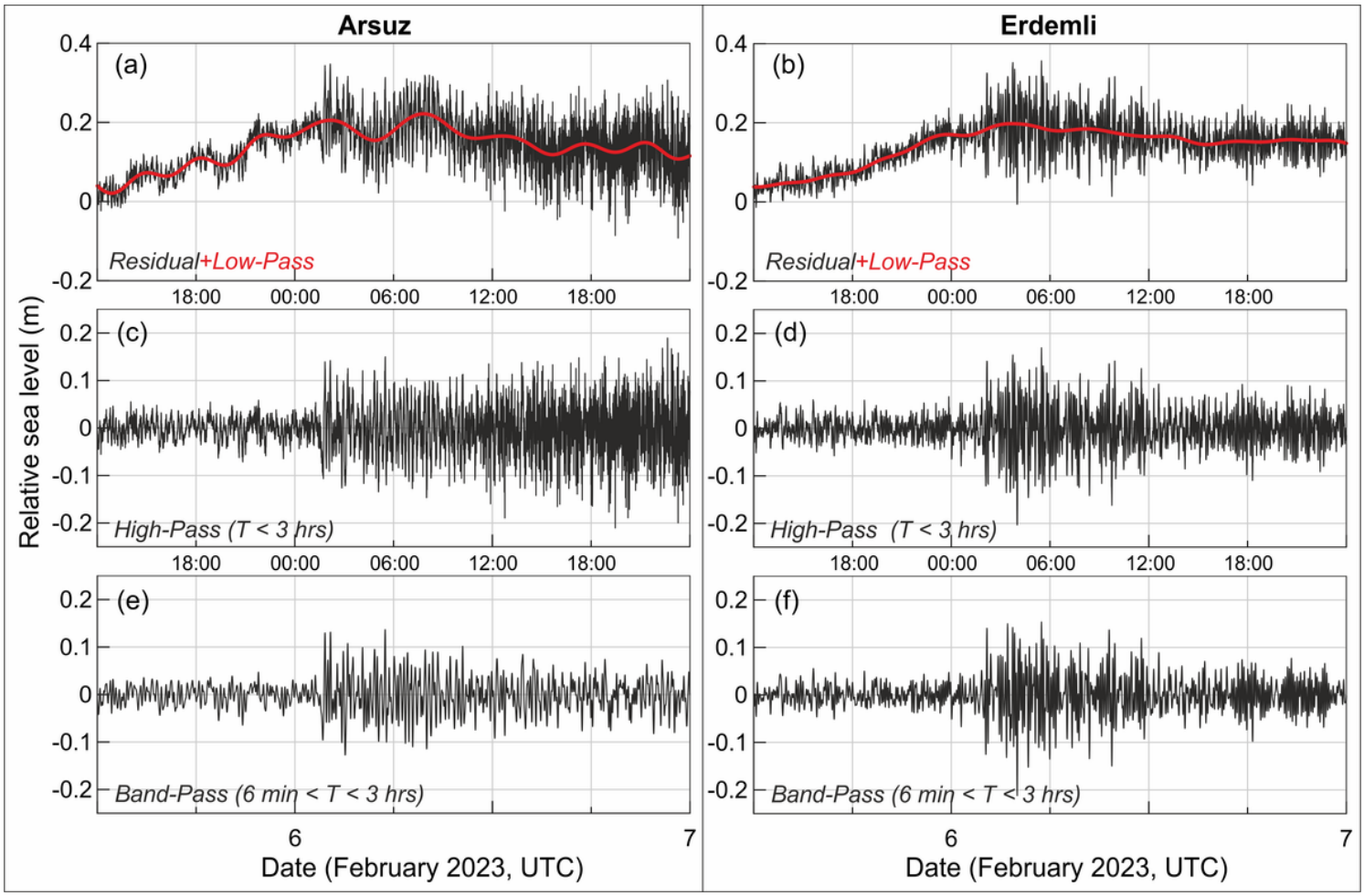


Figure 9

(a–b) Residual sea level records, (c–d) high-frequency sea-level records (ζHF), and (e–f) sea level oscillations (ζ_{bp}) with periods from 6 min to 3 h for the period of 5–7 February 2023 at Arsuz and Erdemli. The solid red line indicates the low-frequency sea level component (storm surges).

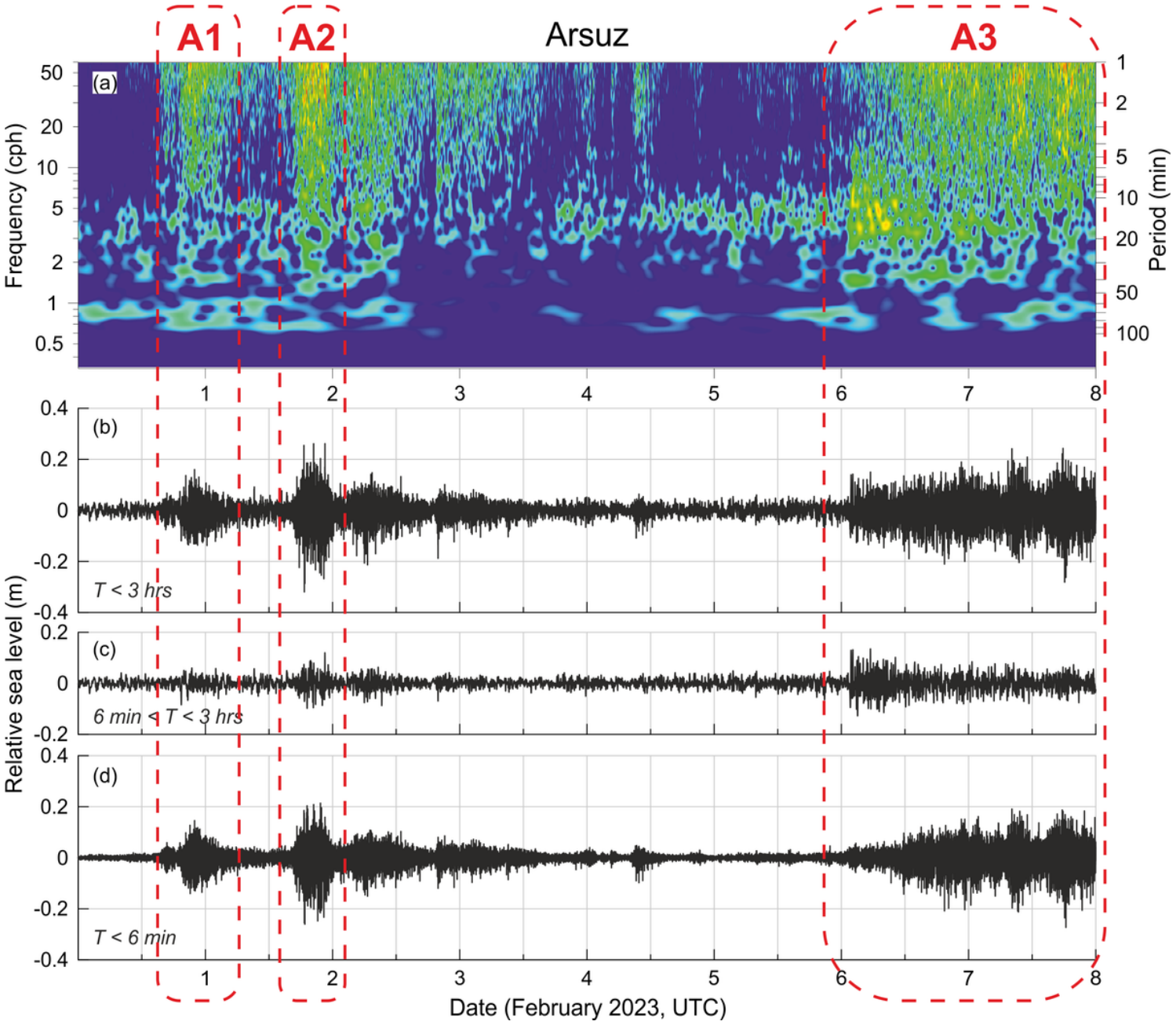


Figure 10

(a) The f-t diagram of the high-frequency sea-level records and time series of (b) the high-frequency sea level records (ζ_{HF}), (c) the narrow-band frequency sea level records (ζ_{bp}), (d) the highest frequency component (ζ_{IG}) at Arsuz from 31 January to 8 February 2023.